analytical chemistry

pubs.acs.org/ac Article

Charge-Transfer Resonance and Surface Defect-Dominated WO_3 Hollow Microspheres as SERS Substrates for the miRNA 155 Assay

Lingling Jiang, Yali Hu, Haina Zhang, Xiliang Luo, Ruo Yuan, and Xia Yang*

Cite This: *Anal. Chem.* 2022, 94, 6967−6975 Read Online

ACCESS | Metrics & More | Article Recommendations | Supporting Information

ABSTRACT: Chemical enhancement with charge transfer (CT) between the adsorbed Raman molecule and the semiconductor mainly contributed to semiconductor surface-enhanced Raman scattering (SERS). In this work, a three-dimensional (3D) WO_3 hollow microsphere is first developed as a SERS-active substrate. This 3D WO_3 has a smaller band gap and rich surface defects compared with flake WO_3. Interestingly, these properties in the WO_3 hollow microspheres lead to an increase in charge transfer, which causes a strong CT interaction between the substrate−Raman molecule interfaces, resulting in a large SERS enhancement. The 3D WO_3 showed an excellent SERS performance with an enhancement factor (EF) of 1.6×10^6. Finally, a SERS biosensor is constructed based on the above-mentioned semiconductor materials, which can be used for the sensitive detection of miRNA 155 with a limit of detection (LOD) of 0.18 fM by employing a catalytic hairpin assembly (CHA) strategy. This work provides important guidance for semiconductor topography design to improve the SERS performance, supplying a new strategy for biomolecular analysis and disease diagnosis.

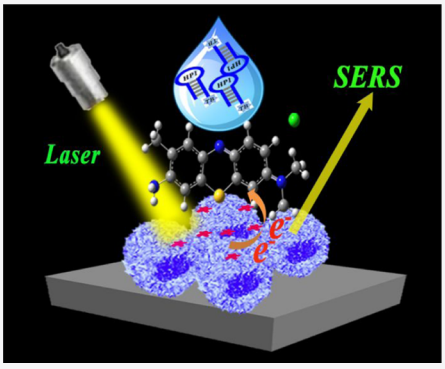

INTRODUCTION

Surface-enhanced Raman spectroscopy (SERS) is a highly sensitive molecular fingerprinting technology,[1,2] which has been widely used in different fields, such as biomedical, pharmaceutical, and life sciences.[3,4] As is known, the enhancement mechanisms of SERS include two types: one is electromagnetic enhancement caused by surface plasma resonance (SPR) and the other one is chemical enhancement of charge transfer (CT) between Raman molecules and the substrate.[5,6] Frequently, precious metals are used as efficient SERS substrates, in which a huge SPR effect is generated to greatly amplify the Raman signal.[7−9] However, they have inherent disadvantages, such as high cost, easy to aggregate, poor biocompatibility, etc.[10] Significantly, semiconductor nanostructures allow more control over parameters such as the exciton Bohr radius, band structure, doping type, crystallinity, and selectivity enhancement, which enable semiconductor substrates to accurately identify target molecules in complex systems.[11] In recent years, developing semiconductor SERS substrates is gradually becoming a research focus.

Since the discovery of semiconductor SERS activities in the 1980s, a large number of SERS-active nanomaterials have been successfully manufactured,[12] from zero- to three-dimensional (3D) materials such as MoO_{3-x} quantum dots,[13] Ta-doped TiO_2 nanofibers,[14] CuTe nanocrystals,[15] ultrathin WO_3 nanostructures,[16] ZnO nanosheets,[17] MXenes,[18] ZnO nanocages,[19] etc. However, in comparison to precious metals, the enhancement factor (EF) of semiconductors is too weak, which limits the application of semiconductor SERS substrates in many areas.[20,21] As of now, to immensely enhance the SERS performance of semiconductors, two methods have been studied: morphological design and elemental doping, which can correspondingly transfer the LSPR peak to the near-infrared or visible region, hence producing some metal-like characters and boosting the SERS activity of the semiconductor.[22] For example, the Cu_2O superstructure[23] and the Mo-doped Ta_2O_5 substrate[24] showed a significant SERS sensitivity due to their surface defects and coupling resonance effect. Nevertheless, among the methods, the operation of elemental doping strategy was complicated, which also brought impurities to the SERS system.

Herein, we used a simple template-free strategy to synthesize 3D WO_3 hollow microspheres assembled by nanosheets (named H-WO_3), which were first used as SERS substrates.[25] This synthesis process did not require a complex defect tuning process and has a narrow band gap and surface defects. These changes occur naturally during the self-aggregation process, which induces an increase in the sub-band-gap states and free electrons, which may promote the resonance coupling and CT processes.[23] Compared with the flake WO_3 (F-WO_3), the H-WO_3 semiconductors with rich surface defects showed a

Received: December 1, 2021
Accepted: March 3, 2022
Published: March 15, 2022

https://doi.org/10.1021/acs.analchem.1c05200
Anal. Chem. 2022, 94, 6967−6975

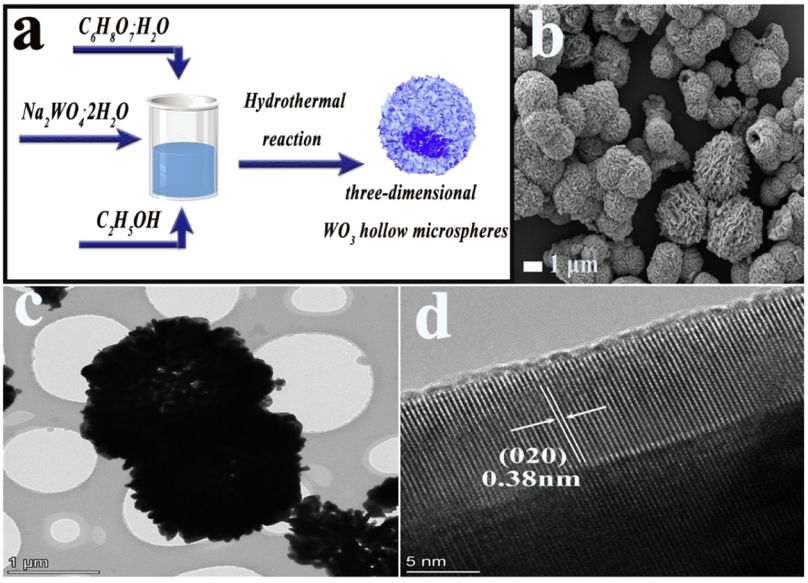

Figure 1. (a) Schematic diagram of synthesizing WO_3 hollow microspheres. (b) SEM image of H-WO_3. (c) TEM image of H-WO_3. (d) HRTEM of H-WO_3.

significant SERS sensitivity with an EF of 1.6×10^6 and a low detection limit of 1×10^{-8} M for toluidine blue (TB) molecules, which was superior to numerous studied semiconductor SERS substrates. The excellent SERS performance enhancement of H-WO_3 can be attributed to (1) its rich surface defects, (2) charge-transfer complex resonating with incident light, and (3) its unique hollow structure and high refractive index characteristics.

MicroRNA (miRNA) is a kind of noncoding single-stranded RNA molecule with about 22 nucleotides encoded by endogenous genes.[26] There is a close relationship between miRNA expression disorders and human diseases. Thus, monitoring the expression level of miRNA is helpful to make it a promising biomarker for the diagnosis, prognosis, and treatment of related diseases and even cancer.[27] In this paper, the H-WO_3 semiconductor was used instead of traditional precious metals as the SERS substrate, and a sensitive biosensor was designed based on a simple CHA amplification strategy, which realized the quantitative detection of the target miRNA 155 with a limit of detection (LOD) of 0.18 fM. This paper offers a new method for the design of novel semiconductor SERS substrates for biomolecular analysis and disease diagnosis.

EXPERIMENTAL SECTION

Preparation of 3D WO_3 Hollow Microspheres and Flake WO_3. A simple hydrothermal method was developed to synthesize WO_3 hollow microspheres. In the first step, 1.0 g of $Na_2WO_4·2H_2O$ and 1.5 g of citric acid were dissolved in 15 mL of distilled water and 5 mL of ethanol and vigorously stirred for 40 min to form a uniform solution. Second, 3 mL of 4 M hydrochloric acid was added to the above solution under stirring. Then, the above solution was transferred to a 50 mL hydrothermal reactor and heated at 120 °C for 18 h after stirring for 10 min. Third, the resulting yellow precipitate was washed twice with deionized and anhydrous ethanol separately and then dried in a 60 °C oven for 10 h and finally annealed in air at 500 °C for 3 h to obtain WO_3 hollow microspheres (H-WO_3).

A total of 1.65 g of $Na_2WO_4·2H_2O$ sample was dissolved in 50 mL of 1 M hydrochloric acid and vigorously stirred at room temperature for 72 h. Then, the products were centrifuged and washed with deionized water until the pH values of the supernatant reached 7. The yellow precipitate ($WO_3·2H_2O$ precursor) was vacuum-dried at room temperature for 12 h. Eventually, the flake WO_3 powder was obtained by calcination at 500 °C in air for 2 h.

Measurement of SERS Performance. All SERS samples were prepared by a conventional immersion procedure. Normally, using the WO_3 hollow microsphere system as an example, 2 mg of the powder sample is added into 1 mL of toluidine blue (TB) aqueous solution of the desired concentration and allowed to soak for 30 min. The mixture was then centrifuged, and the precipitate was transferred to a clean Si wafer and dried at 60 °C. For blank samples, 20 μL of TB solutions was simply dropped onto a clean Si wafer and dried at 60 °C. The Raman spectra were collected by a Raman spectrometer (Renishaw InVia Raman spectrometer, InVia, U.K.) with the equipment of a 532 nm He−Ne laser (0.25 mW, of power on the 50× objective). The laser spot was 1.3 μm in diameter. The exposure time was 1 s.

Target-Triggered Catalytic Hairpin Assembly (CHA) Amplification. The CHA reactions were prepared by mixing 10 μL of HP1 modified with TB and 10 μL of HP2 modified with magnetic beads with series concentrations of miRNA 155 and then incubated at 37 °C for 2 h.

Preparation of the 155 Biosensor. First, the Raman signal of the above mixed solution was measured on the H-WO_3 substrate without adding the target miRNA 155. Then, the target miRNA 155 was added into the above mixed solution to achieve target-triggered CHA amplification. After magnetic separation, the supernatant was used to measure the Raman signal with WO_3 hollow microspheres as substrates. The detection of miRNA 155 was completed based on the difference between the two signals.

https://doi.org/10.1021/acs.analchem.1c05200
Anal. Chem. 2022, 94, 6967−6975

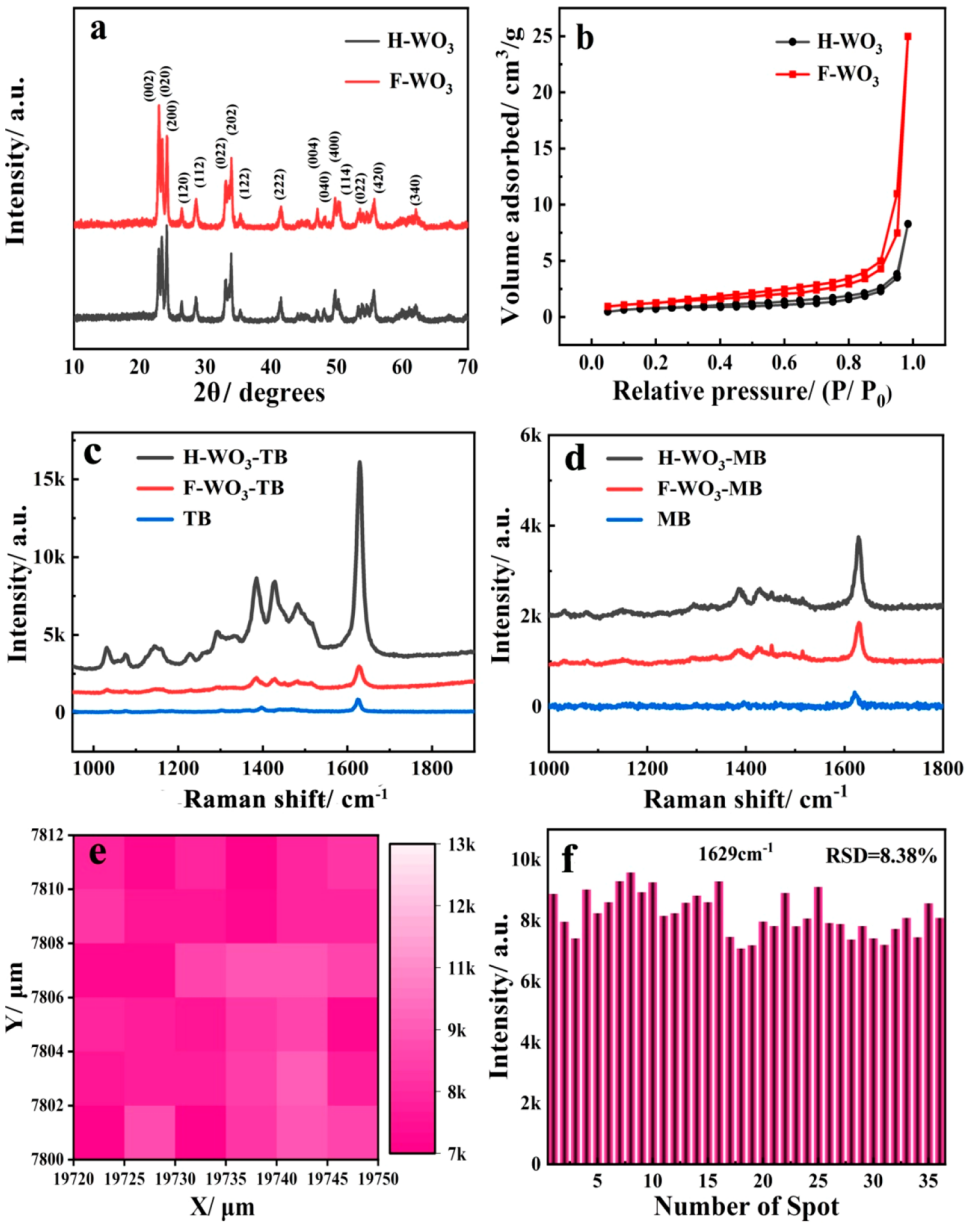

Figure 2. (a) XRD patterns of H-WO_3 and F-WO_3 samples. (b) BET results of H-WO_3 and F-WO_3. (c) Raman spectra of TB (1.0×10^{-5} M) on H-WO_3, F-WO_3, and Si wafer. (d) Raman spectra of MB (1.0×10^{-5} M) on H-WO_3, F-WO_3, and Si wafer. (e) SERS mapping measurements. (f) SERS intensity fluctuation of the 1629 cm^{-1} SERS peak from 36 randomly chosen SERS spectra when using H-WO_3 as the SERS substrate to detect 0.5×10^{-5} M TB.

RESULTS AND DISCUSSION

Material Characterization. The shape-controlled H-WO_3 was synthesized via a simple hydrothermal reaction according to the literature,[28] as shown in Figure 1a. This method is efficient and simple without needing any traditional synthesis process like template or acid treatment. The SEM micrographs of H-WO_3 are shown in Figure 1b, which clearly indicate that many nanosheets are assembled and each hollow microsphere is ~2 to 3 μm. The SEM micrograph of flake WO_3 (F-WO_3) compared with H-WO_3 is shown in Figure S3a,b. The TEM of H-WO_3 is clearly observed in Figure 1c. The lattice fringe spacing of H-WO_3 is 0.38 nm, as seen from Figure 1d, anastomosing to the (020) plane of WO_3 (JCPDS No. 72-1465).

The crystal phase of H-WO_3 and F-WO_3 was authenticated by XRD, as shown in Figure 2a. The diffraction peaks of both materials are in good agreement with standard WO_3 (JCPDS No. 72-1465), and there is no impurity phase in the XRD spectrum, indicating the high purity of the as-prepared WO_3.[29] Figure 2b shows the Brunauer–Emmett–Teller (BET) N_2 adsorption–desorption curves, which exhibited that the specific surface areas (SSAs) of the WO_3 hollow microspheres and flake WO_3 were 3.133 and 4.537 $m^2\ g^{-1}$, respectively, indicating that the BET has no difference for these two kinds of materials.

SERS Performance and Enhanced Mechanism of H-WO_3. The Raman molecular TB and methylene blue (MB) were used as Raman probe molecules to measure the Raman performance of H-WO_3 and F-WO_3, respectively, as shown in Figure 2c,d. It can be clearly seen that compared with the F-

https://doi.org/10.1021/acs.analchem.1c05200
Anal. Chem. 2022, 94, 6967−6975

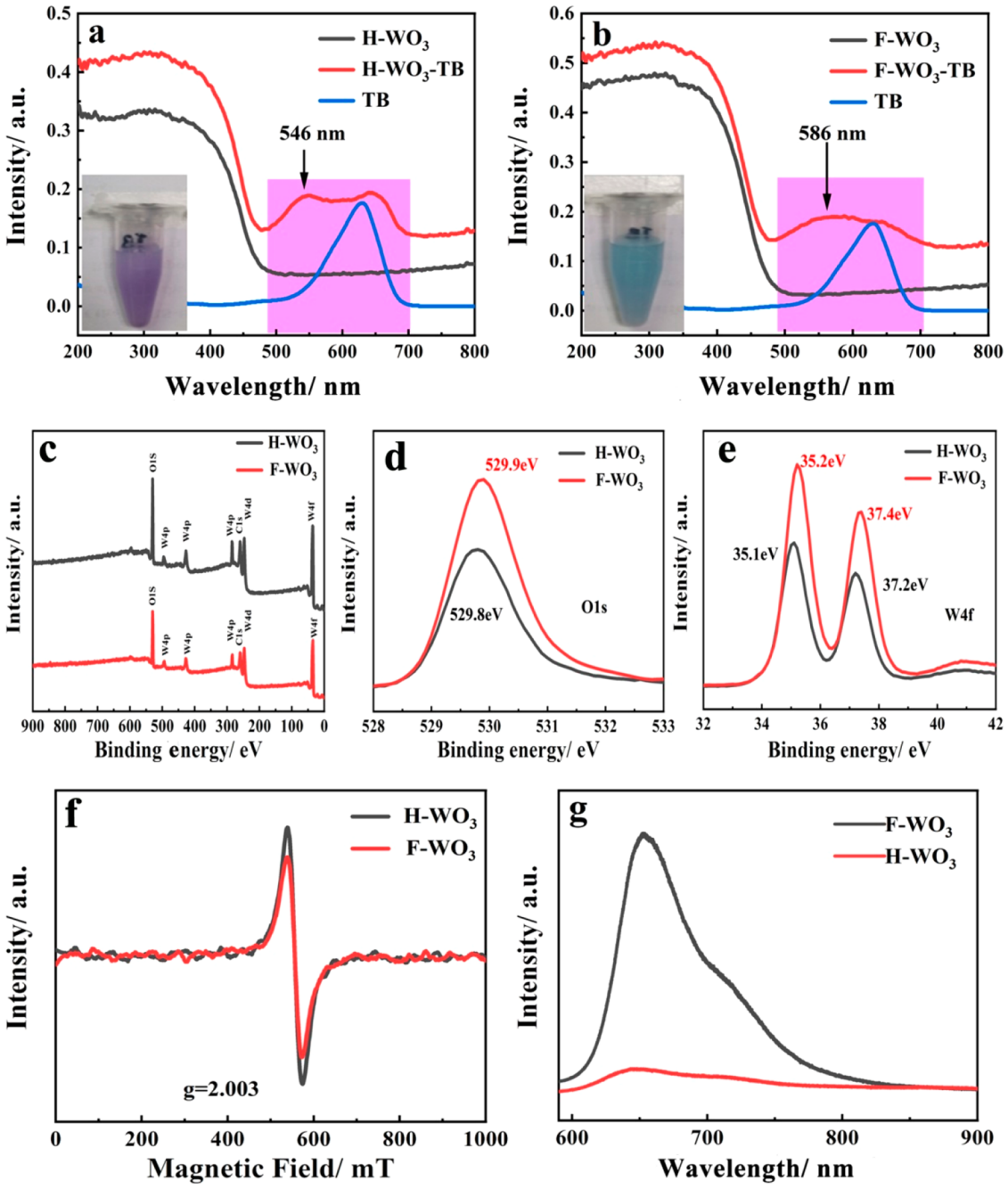

Figure 3. (a) UV−vis absorption spectra of H-WO_3 powders, TB-modified H-WO_3 powders, and TB solution; the inset shows the picture of quantitative H-WO_3 soaked in TB solution for 3 h. (b) UV−vis absorption spectra of F-WO_3 powders and TB-modified F-WO_3 powders in TB solution; the inset shows the picture of quantitative F-WO_3 soaked in TB solution for 3 h. (c) XPS survey, (d) O 1s, and (e) W 4f XPS spectra in H-WO_3 and F-WO_3 substrates. (f) Electron spin resonance (ESR) spectra of H-WO_3 and F-WO_3. (g) PL spectra of H-WO_3 and F-WO_3.

WO_3 substrate, H-WO_3 has a stronger enhancement effect for TB molecules with a surface enhancement factor (EF) of 1.6×10^6 (see Supporting Information for details) at the Raman peak 1629 cm^{-1}. On the contrary, this enhancement effect is not obvious for MB. The 30 μm × 12 μm SERS area mapping reflected an SERS intensity fluctuation of 1.0×10^{-5} M TB at 1629 cm^{-1} with step sizes of 5 and 2 μm, as shown in Figure 2e, and the relative standard deviation (RSD) of the SERS intensity is 8.38% (Figure 2f). Next, we measured the sensitivity of the SERS platform with H-WO_3 as the SERS substrate and TB (10^{-8}−10^{-4} M) as the probe molecule (Figure S1). Compared with other semiconductor SERS substrates, our SERS substrate showed excellent enhanced performance (Table S3).

Considering that H-WO_3 has low intrinsic carrier density and negligible plasmon resonances, the significant Raman enhancement observed for H-WO_3 is unlikely to be from electromagnetic mechanisms. First, we analyzed the contribution of chemical enhancement (including CT resonance) on the SERS performance of H-WO_3 substrates. The UV−vis absorption spectra (Figure 3a,b) of the TB molecule adsorbed on H-WO_3 and F-WO_3 were compared with the spectra of the pure materials and TB solutions (638 nm); new absorption peaks at about 546 and 586 nm and a certain degree of peak

https://doi.org/10.1021/acs.analchem.1c05200
Anal. Chem. 2022, 94, 6967−6975

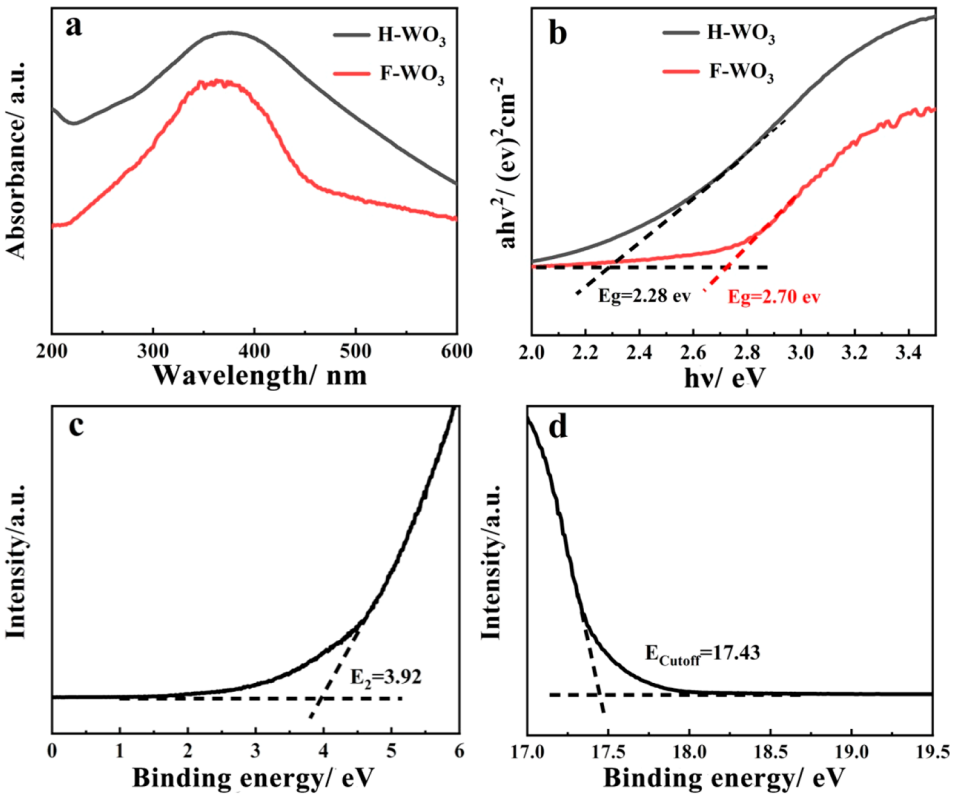

Figure 4. (a) UV−vis absorption spectra of H-WO_3 and F-WO_3. (b) Corresponding plots of $(ah\upsilon)^2$ versus hυ. (c, d) UPS spectra of H-WO_3.

broadening appeared in the composite absorption spectrum. This is because the strong absorption of visible light of TB can effectively expand the light absorption range of the large band-gap semiconductor from the ultraviolet to visible-light region after the TB dye is adsorbed on the semiconductor surface.[30] Moreover, it resonates with the incident light (532 nm), which suggested that a CT process and a strong chemical interaction might happen between H-WO_3 and the TB molecule. Besides, the color difference in the inset image also indicates that there is an intense chemical mutual effect between the H-WO_3 substrate and the TB probe molecule.

Furthermore, Fourier transform infrared (FTIR) (Figure S4) has an absorption peak at 1636 cm^{-1}, matching with the vibration peak of the benzene ring in the TB molecule, so the interaction between the base and the dye molecules was further proved. The SERS intensity is proportional to polarizability (α) of the Raman dye, which depends on the strength of electron−phonon coupling and the resonance conditions.[31] The reason is that the ground-state electrons obtain sufficient energy by absorbing the incident light at a certain laser wavelength, and then, these excited electrons are moved to the molecule through the coupling energy level, which enhances the polarizability of the molecule, leading to chemical enhancement. Figure S5 shows that the enhancement of the TB molecule on H-WO_3 under the excitation of 532 (closer to 546 nm) nm was obviously greater than that at 633 nm (further away from 546 nm). It is well explained by resonance effects, i.e., the chemical enhancement results of the quasi-resonance Raman scattering effect between the CT complex (substrates and probe molecules) and the excitation wavelength ($\lambda_{CT} \approx \lambda_{laser}$).

The surface/near-surface chemical compositions of H-WO_3 and F-WO_3 were examined by X-ray photoelectron spectroscopy (XPS). The full-range XPS spectra (Figure 3c) of H-WO_3 and F-WO_3 manifested that W and O are primary elements in the materials. Figure 3d shows that the binding energies of these peaks of O 1s locate from 529.9 to 529.8 eV, and Figure 3e reveals that the binding energies of these peaks of W $4f_{7/2}$ are from 35.2 to 35.1 eV and for W4 $f_{5/2}$ they are from 37.4 to 37.2 eV. The XPS peaks of O 1s and W 4f orbitals of the H-WO_3 structure move to lower binding energy levels in comparison to F-WO_3, which can be ascribed to photoelectrons emitted from the lower oxidation states of tungsten (substoichiometric WO_{3-x}). It indicates that incremental surface defect or incomplete W−O bonding existed during the nanosheet-assembled WO_3 hollow microspheres.[32] The electron spin resonance (ESR) spectra were also collected to provide more evidence for probing vacancy defects (Figure 3f). A sharp signal was observed at g = 2.003, which corresponds to the unpaired electrons[33] and further testifies the presence of vacancy defects in the heterostructure. Besides, Figure 3g presents the photoluminescence (PL) spectra of H-WO_3 and F-WO_3. The two samples include emission bands with a wide deep-level emission (DLE) from 600 to 780 nm, which is due to inherent defects such as oxygen vacancies or various surface states. The DLE peak intensity of F-WO_3 is stronger than H-WO_3 owing to the new energy levels produced under the conduction band as electron traps, which inhibit the photoexcitation-induced charge recombination.[34] It indicated that more surface defects are generated in H-WO_3. The above conclusions played an indispensable role in promoting the efficient CT process between the semiconductor material and the adsorptive TB molecule, which may further enhance the SERS signal.

From the UV−vis adsorption and the UPS valence states on H-WO_3 and F-WO_3, information on the band gap, valence

https://doi.org/10.1021/acs.analchem.1c05200
Anal. Chem. 2022, 94, 6967−6975

Scheme 1. (a) Photo-Induced Charge-Transfer Process between H-WO_3 and TB and (b) Photo-Induced Charge-Transfer Process between F-WO_3 and TB.

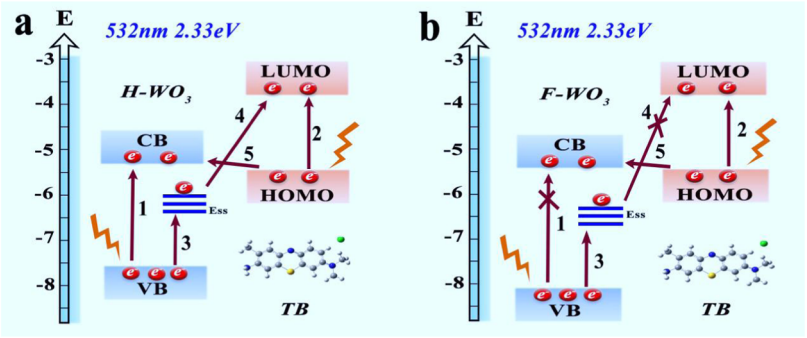

Scheme 2. (A) Raman Spectra of the Solution without the Target and with the Target miRNA 155, (B) Target-miRNA-Triggered CHA Amplification Strategy for Biosensors, and (C) Schematic Diagram of the SERS Biosensor

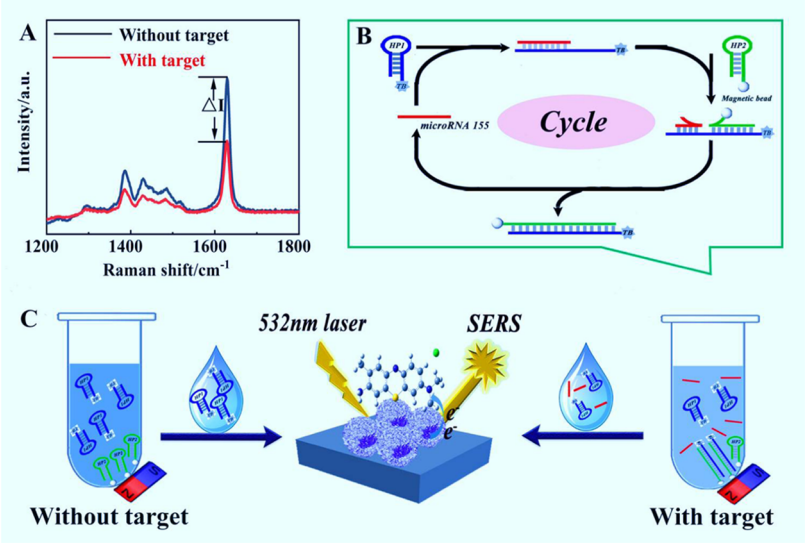

band (VB), and conduction band (CB) of the two samples can be obtained. Figure 4a,b shows the UV−vis spectra and the plots of $(\alpha h\nu)^{1/2}$ against $h\nu$. According to the Tauc equation,[35] the band gaps of H-WO_3 and F-WO_3 are 2.28 and 2.70 eV, respectively. The work function obtained from the ultraviolet photoelectron spectroscopy (UPS) (Figure 4c,d) of H-WO_3 is 3.79 eV ($W_f = h\nu - E_{cutoff}$), the VB is situated at 7.71 eV (VB = $W_f + E_2$), and the CB is situated at 5.43 eV (CB = VB − E_g). Similarly, the work function obtained from the UPS (Figure S6a,b) of F-WO_3 is 5.21 eV, the VB is situated at 8.19 eV, and CB is at 5.49 eV.

The lowest unoccupied molecular orbital (LUMO) and the highest occupied molecular orbital (HOMO) of TB were measured by electrochemical and optical methods. The E_g of TB was 1.86 eV; the HOMO and LUMO of TB were calculated to be −5.57 and −3.71 eV, respectively (see Figure S7 for details). The possibility of electron transition between the semiconductor and the Raman molecule will be magnified markedly because of the presence of abundant surface vacancy defect states. Scheme 1 shows the CT process between the TB molecule and H-WO_3 and F-WO_3. The energy provided by the 532 nm laser is 2.33 eV. For the H-WO_3 substrates and the TB probe molecular system, the charge-transfer processes that can occur include routes 1−5 (Scheme 1a); however, for the F-WO_3 substrates and the TB probe molecular system, the CT cannot occur in process 1 and process 4 (Scheme 1b). To quantify the CT contribution to SERS, on account of the intense surface interaction, the CT contribution of H-WO_3 to the SERS signal of TB proved to be higher than that of F-WO_3 (Figure S2b), which could be quantified using this equation $\rho_{CT}(k) = \frac{I^k(CT) - I^k(SPR)}{I^k(CT) + I^0(SPR)}$.[36,37] Among them, the degrees of CT for TB on H-WO_3 and F-WO_3 are calculated to be 0.81 and 0.70, respectively (calculation details in the Supporting Information, Figure S2 and Table S2). This result indicates that the CT contribution of H-WO_3 is higher than that of F-WO_3, and the CT mechanism is the main SERS enhancement of this semiconductor. In addition, there might be another reason for the enhancement: the laser can be reflected multiple times in the hollow cavity of the material due to the material's high refractive index properties,[38] which increases the utilization of light and further enhances the Raman signal since the material is hollow and microspherical. In short, the excellent SERS performance enhancement of H-WO_3 can be attributed to (1) its rich surface defects, (2) charge-transfer complex resonating with incident light, and (3) its unique hollow structure and high refractive index characteristics.

Biosensors for the Detection of miRNA 155. As shown in Scheme 2, the target miRNA 155 hybridizes with the external toehold of HP1-TB, which will initiate the unfolding

https://doi.org/10.1021/acs.analchem.1c05200
Anal. Chem. 2022, 94, 6967−6975

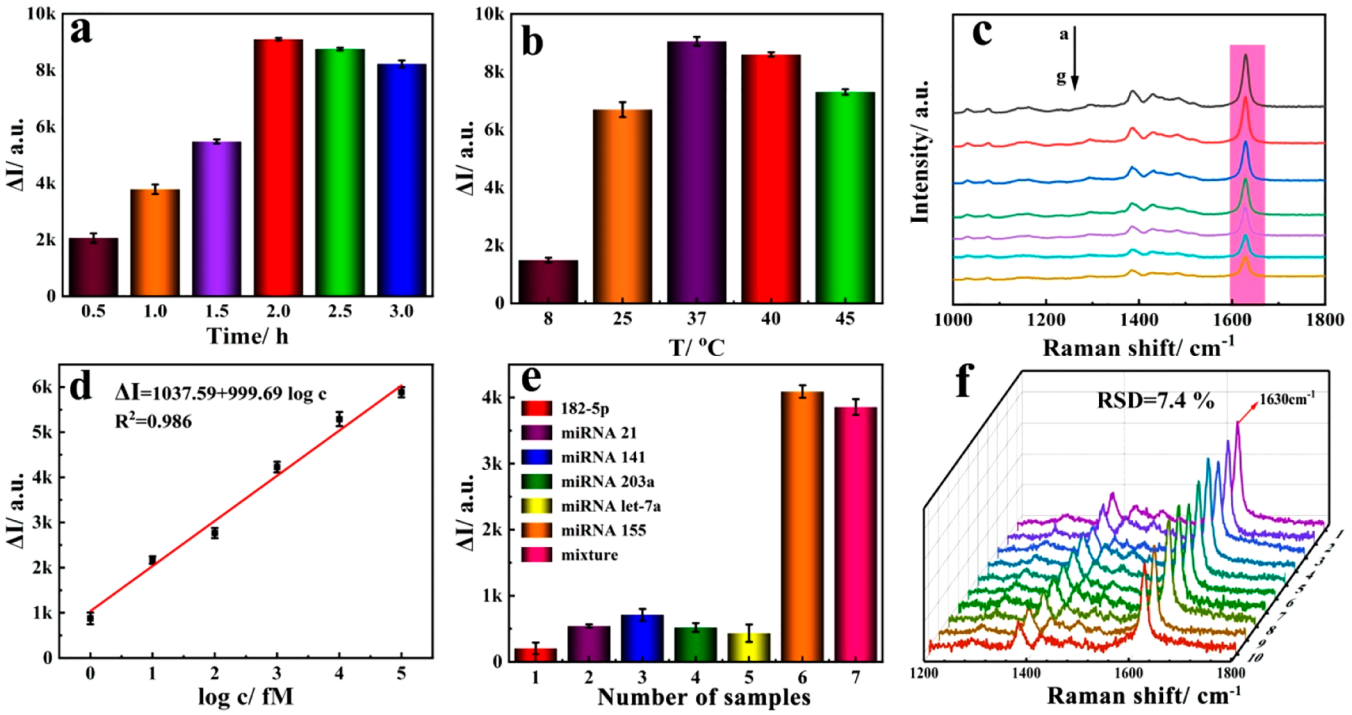

Figure 5. (a) Influence of ΔI with various incubating times. (b) Influence of ΔI with various incubating temperatures. (c) SERS responses on H-WO_3 with the proposed method after incubation of miRNA 155 concentrations from (a) to (g) (0 M, 1 fM to 100 pM) of miRNA 155. (d) Calibration plot of SERS intensity versus the logarithm of miRNA 155 concentration. (e) Selectivity of the Raman biosensor for the target miRNA 155 and other miRNA (including 182−5p, miRNA 21, miRNA 141, miRNA 203a, and miRNA let-7a). (f) SERS spectra measured from 10 different spots on the same SERS platform.

Table 1. Comparison of This Study with Other Works

detection method	detection target	detection limit	linear range	refs
SERS	miRNA 155	0.18 fM	1×10^0−1×10^5 fM	this work
electrochemistry	miRNA 155	67 pM	2.5×10^2−1×10^6 pM	39
fluorescence	miRNA 155	21.7 fM	1×10^2−1×10^8 fM	36
ECL	miRNA 155	5.7 fM	1×10^1−1×10^8 fM	40
SERS	miRNA 155	1.45 fM	1×10^2−5×10^6 fM	41
SERS	miRNA 155	0.67 fM	1×10^0−1×10^7 fM	42

of HP2-TB through a strand displacement process. Whereafter, the open-loop HP1-TB hybridized with the external toehold of HP2 attached to the magnetic beads, leading to the release of target miRNA 155 and the production of HP1/HP2 duplex. The more target miRNA 155 there are, the less TB remains in the upper solution after magnetic separation. In addition, the difference in Raman strength ($\Delta I = I_{blank} - I$, where I_{blank} represents the Raman strength of the solution without the target and I represents the Raman strength of the supernatant after magnetic separation with the target miRNA 155) is proportional to the target miRNA 155. In this way, the sensitive detection of miRNA 155 can be realized using the above-mentioned H-WO_3 as the substrate.

The feasibility of the target-miRNA-triggered CHA reactions was first proved by 15% native PAGE. In Figure S8, the bands of HP1 (lane 1) and HP2 (lane 2) can be clearly observed, and when they are mixed together (lane 3), no cross-reaction bands appear. This is attributed to intramolecular hybridization, which effectively blocks spontaneous hybridization between HP1 and HP2. When HP1 or HP2 was incubated with miRNA 155, HP1 was opened by hybridization with miRNA 155 and led to the formation of miRNA 155/HP1 hybridization (lane 4), which had no obvious difference from the single HP1 (lane 1) band because of the number of bases in the miRNA 155/HP1 hybrid band and the HP1 band has little obvious difference. Lane 5 showed that the miRNA 155 and HP2 had no cross-reaction. However, when miRNA 155/HP1 was incubated with HP2, a significantly lower mobility band (lane 6) was observed, indicating that HP1 and HP2 were self-assembled double-stranded. The above results confirmed that the hybridization between HP1 and HP2 was catalyzed by the target miRNA 155.

Figures 5a,b and S9a,b, respectively, show the relationship between the ΔI and the CHA incubation time and the temperature. It clearly indicates that the best CHA incubation time is about 2 h and the best CHA incubation temperature is about 37°C. Next, different concentrations of miRNA 155 were detected under the experimental conditions of the optimal incubation temperature of 37 °C and the optimal incubation time of 2 h. In the concentration range of 1 fM to 100 pM, Figure 5c,d shows a good linear correlation; the linear equation is $\Delta I = 1037.59 + 999.69 \log c$ (fM), with a correlation coefficient square (R^2) of 0.986 (c is the concentration of miRNA 155). The LOD of the SERS platform is 0.18 fM (the details are in the Supporting Information). We also employed F-WO_3 as the SERS substrate

https://doi.org/10.1021/acs.analchem.1c05200
Anal. Chem. 2022, 94, 6967−6975

instead of H-WO_3 to detect miRNA 155 (Figure S10). Compared with H-WO_3 as the SERS substrate, we could see that the detection range was narrow and the detection limit was worse because the SERS-enhanced performance of F-WO_3 was weak, resulting in lower biosensor sensitivity. Thus, H-WO_3 has a better sensing performance due to its more excellent SERS properties. In addition, compared to other works, our semiconductor SERS platform provided better performance for detection of miRNA 155 (Table 1).

To verify the high selectivity of the SERS biosensor for miRNA 155 detection, we detected the system containing miRNA 21, miRNA 141, miRNA 203a, and let-7a under the same experimental conditions. Figure 5e shows the results of a biosensor used to detect interfering miRNA. It can be seen that the weak Raman strength of interference is basically consistent with that of the blank test (Figure S9c). As shown in Figure 5f, to analyze the reproducibility of the SERS biosensor with the concentration of miRNA 155 (1 pM), we measured 10 different points on the same platform. The relative standard deviation (RSD) of the Raman intensity at 1630 cm^{-1} was 7.4%. Figure S9d shows the Raman spectrum of the sample and five parallel SERS platforms with the 1 pM miRNA 155. The RSD was 3.5% at 1630 cm^{-1}, indicating that the biosensor had good stability.

To prove the applicability of the proposed sensor for detection in actual samples, miRNA 155 from different cancer cell lines, HeLa (cervical cancer cells), and MDA-MB-231 (human breast cancer cells) were analyzed by this SERS biosensor. As shown in Figure S11, when the biosensor was incubated with miRNA samples extracted from HeLa and MDA-MB-231, it was observed that the Raman response was significantly enhanced, and the expression level of MDA-MB-231 is higher than that of HeLa, which is very consistent with previous reports;[43−45] this indicated that the SERS biosensor had outstanding potential in practical application.

CONCLUSIONS

In conclusion, the nanosheet-assembled three-dimensional (3D) WO_3 hollow microspheres have a significantly improved SERS effect. The surface vacancy defect and the resonant coupling between the charge transfer and the incident light, as well as the unique hollow structure and high refractive index properties, further enhanced the Raman scattering effect. The SERS biosensor based on H-WO_3 was used to sensitively detect the target miRNA 155 with the CHA signal amplification strategy. In short, this work provides a new breakthrough and perspective for designing a semiconductor SERS substrate and platform for biomolecular analysis.

ASSOCIATED CONTENT

Supporting Information

The Supporting Information is available free of charge at https://pubs.acs.org/doi/10.1021/acs.analchem.1c05200.

Additional experimental details, SEM image of flake WO_3, UPS spectra of F-WO_3, FTIR of H-WO_3 and F-WO_3 after TB adsorption, native PAGE analysis of miRNA 155-triggered CHA reaction, Raman spectra measured from 532 and 633 nm, TB at concentrations ranging from 10^{-8} to 10^{-4} M collected on H-WO_3 and TB (10^{-2} M) collected on Si, energy-level calculation of toluidine blue, SERS response of the proposed biosensor in HeLa and MDA-MB-231 cells, and calculation of the enhancement factor and detection limit (PDF)

AUTHOR INFORMATION

Corresponding Author

Xia Yang − *Key Laboratory of Luminescence Analysis and Molecular Sensing, Ministry of Education, College of Chemistry and Chemical Engineering, Southwest University, Chongqing 400715, P. R. China;* orcid.org/0000-0003-0897-2106; Email: xiayang2@swu.edu.cn

Authors

Lingling Jiang − *Key Laboratory of Luminescence Analysis and Molecular Sensing, Ministry of Education, College of Chemistry and Chemical Engineering, Southwest University, Chongqing 400715, P. R. China*

Yali Hu − *Key Laboratory of Luminescence Analysis and Molecular Sensing, Ministry of Education, College of Chemistry and Chemical Engineering, Southwest University, Chongqing 400715, P. R. China*

Haina Zhang − *Key Laboratory of Luminescence Analysis and Molecular Sensing, Ministry of Education, College of Chemistry and Chemical Engineering, Southwest University, Chongqing 400715, P. R. China*

Xiliang Luo − *Shandong Key Laboratory of Biochemical Analysis, College of Chemistry and Molecular Engineering, Qingdao University of Science and Technology, Qingdao 266042, P. R. China; Key Laboratory of Sensor Analysis of Tumor Markers, Ministry of Education, College of Chemistry and Molecular Engineering, Qingdao University of Science and Technology, Qingdao 266061, P. R. China;* orcid.org/0000-0001-6075-7089

Ruo Yuan − *Key Laboratory of Luminescence Analysis and Molecular Sensing, Ministry of Education, College of Chemistry and Chemical Engineering, Southwest University, Chongqing 400715, P. R. China;* orcid.org/0000-0003-3664-6236

Complete contact information is available at: https://pubs.acs.org/10.1021/acs.analchem.1c05200

Author Contributions

All authors have given approval to the final version of the manuscript.

Notes

The authors declare no competing financial interest.

ACKNOWLEDGMENTS

This work was supported by the National Natural Science Foundation (22174114) and the Chongqing Research Program of Basic Research and Frontier Technology (cstc2019jcyj-msxmX0209).

REFERENCES

(1) Wen, B. Y.; Wang, A.; Lin, J. S.; Guan, P. C.; Radjenovic, P. M.; Zhang, Y. J.; Tian, Z. Q.; Li, J. F. *Small Methods* **2021**, *5*, No. 2000993.

(2) Alessandri, I.; Lombardi, J. R. *Chem. Rev.* **2016**, *116*, 14921−14981.

(3) Lee, H. K.; Lee, Y. H.; Koh, C. S. L.; Phan-Quang, G. C.; Han, X.; Lay, C. L.; Sim, H. Y. F.; Kao, Y.; An, Q.; Ling, X. Y. *Chem. Soc. Rev.* **2019**, *48*, 731−756.

(4) Huang, Z.; Meng, G.; Hu, X.; Pan, Q.; Huo, D.; Zhou, H.; Ke, Y.; Wu, N. *Nano Res.* **2019**, *12*, 449−455.

(5) Willets, K. A. *Chem. Soc. Rev.* **2014**, *43*, 3854−3864.
(6) Cao, Z.; He, P.; Huang, T.; Yang, S.; Han, S.; Wang, X.; Ding, G. *Chem. Mater.* **2020**, *32*, 3813−3822.
(7) Chen, J.; Liu, G.; Zhu, Y.; Su, M.; Yin, P.; Wu, X.; Lu, Q.; Tan, C.; Zhao, M.; Liu, Z.; et al. *J. Am. Chem. Soc.* **2020**, *142*, 7161−7167.
(8) Yang, Y.; Peng, Y.; Lin, C.; Long, L.; Hu, J.; He, J.; Zeng, H.; Huang, Z.; Li, Z.; Tanemura, M.; et al. *Nano−Micro Lett.* **2021**, *13*, No. 52.
(9) De Marchi, S.; Vázquez-Iglesias, L.; Bodelón, G.; Pérez-Juste, I.; Fernández, L. A.; Pérez-Juste, J.; Pastoriza-Santos, I. *Chem. Mater.* **2020**, *32*, 5739−5749.
(10) Zheng, Z.; Cong, S.; Gong, W.; Xuan, J.; Li, G.; Lu, W.; Geng, F.; Zhao, Z. *Nat. Commun.* **2017**, *8*, No. 1993.
(11) Karthick Kannan, P.; Shankar, P.; Blackman, C.; Chung, C. H. *Adv. Mater.* **2019**, *31*, No. 1803432.
(12) Wang, X.; Guo, L. *Angew. Chem., Int. Ed.* **2020**, *132*, 4259−4267.
(13) Zhang, J.; Pan, Y.; Chen, Y.; Lu, H. *J. Mater. Chem. C* **2018**, *6*, 2216−2220.
(14) Singh, N.; Prakash, J.; Misra, M.; Sharma, A.; Gupta, R. K. *ACS Appl. Mater. Interfaces* **2017**, *9*, 28495−28507.
(15) Li, W.; Zamani, R.; Rivera Gil, P.; Pelaz, B.; Ibáñez, M.; Cadavid, D.; Shavel, A.; Alvarez-Puebla, R. A.; Parak, W. J.; Arbiol, J.; et al. *J. Am. Chem. Soc.* **2013**, *135*, 7098−7101.
(16) Song, G.; Gong, W.; Cong, S.; Zhao, Z. *Angew. Chem., Int. Ed.* **2021**, *60*, 5505−5511.
(17) Lin, J.; Yu, J.; Akakuru, O. U.; Wang, X.; Yuan, B.; Chen, T.; Guo, L.; Wu, A. *Chem. Sci.* **2020**, *11*, 9414−9420.
(18) Peng, Y.; Lin, C.; Long, L.; Masaki, T.; Tang, M.; Yang, L.; Liu, J.; Huang, Z.; Li, Z.; Luo, X.; et al. *Nano−Micro Lett.* **2021**, *13*, No. 52.
(19) Wang, X.; Shi, W.; Jin, Z.; Huang, W.; Lin, J.; Ma, G.; Li, S.; Guo, L. *Angew. Chem., Int. Ed.* **2017**, *56*, 9851−9855.
(20) Gu, C.; Li, D.; Zeng, S.; Jiang, T.; Shen, X.; Zhang, H. *Nanoscale* **2021**, *13*, 5620−5651.
(21) Dong, J.; Huang, J.; Wang, A.; Biesold-McGee, G. V.; Zhang, X.; Gao, S.; Wang, S.; Lai, Y.; Lin, Z. *Nano Energy* **2020**, *71*, No. 104579.
(22) Ji, W.; Li, L.; Song, W.; Wang, X.; Zhao, B.; Ozaki, Y. *Angew. Chem., Int. Ed.* **2019**, *58*, 14452−14456.
(23) Lin, J.; Shang, Y.; Li, X.; Yu, J.; Wang, X.; Guo, L. *Adv. Mater.* **2017**, *29*, No. 1604797.
(24) Yang, L.; Peng, Y.; Yang, Y.; Liu, J.; Huang, H.; Yu, B.; Zhao, J.; Lu, Y.; Huang, Z.; Li, Z.; et al. *Adv. Sci.* **2019**, *6*, No. 1900310.
(25) Zhai, C.; Zhu, M.; Jiang, L.; Yang, T.; Zhao, Q.; Luo, Y.; Zhang, M. *Appl. Surf. Sci.* **2019**, *463*, 1078−1084.
(26) Brancati, G.; Großhans, H. *Nucleic Acids Res.* **2018**, *46*, 3259−3269.
(27) Yang, C.; Pourhassan-Moghaddam, M.; Wu, L.; Bai, P.; Thierry, B. *ACS Sens.* **2017**, *2*, 635−640.
(28) Chen, D.; Ye, J. *Adv. Funct. Mater.* **2008**, *18*, 1922−1928.
(29) Song, L.; Yang, S.; Wei, W.; Qu, P.; Xu, M.; Liu, Y. *Sci. Bull.* **2015**, *60*, 892−895.
(30) He, X.; Zhang, C. *J. Mater. Sci.* **2019**, *54*, 8831−8851.
(31) Sun, H.; Yao, M.; Liu, S.; Song, Y.; Shen, F.; Dong, J.; Yao, Z.; Zhao, B.; Liu, B. *ACS Appl. Mater. Interfaces* **2021**, *13*, 26551−26560.
(32) Wang, Y.; Liu, B.; Xiao, S.; Wang, X.; Sun, L.; Li, H.; Xie, W.; Li, Q.; Zhang, Q.; Wang, T. *ACS Appl. Mater. Interfaces* **2016**, *8*, 9674−9683.
(33) Li, J.; Xu, X.; Huang, B.; Lou, Z.; Li, B. *ACS Appl. Mater. Interfaces* **2021**, *13*, 10047−10053.
(34) Yang, S.; Yao, J.; Quan, Y.; Hu, M.; Su, R.; Gao, M.; Han, D.; Yang, J. *Light: Sci. Appl.* **2020**, *9*, No. 117.
(35) Sun, H.; Cong, S.; Zheng, Z.; Wang, Z.; Chen, Z.; Zhao, Z. *J. Am. Chem. Soc.* **2019**, *141*, 870−878.
(36) Cong, S.; Wang, Z.; Gong, W.; Chen, Z.; Lu, W.; Lombardi, J. R.; Zhao, Z. *Nat. Commun.* **2019**, *10*, 678−687.
(37) Xiao, G.; Man, S. *Chem. Phys. Lett.* **2007**, *447*, 305−309.
(38) Alessandri, I. *J. Am. Chem. Soc.* **2013**, *135*, 5541−5544.
(39) Li, C.; Chen, Z.; Zhang, Y.; He, J.; Yuan, R.; Xu, W. *Anal. Chem.* **2020**, *92*, 13369−13377.
(40) Wang, F.; Liu, Y.; Fu, C.; Li, N.; Du, M.; Zhang, L.; Ge, S.; Yu, J. *Anal. Chem.* **2021**, *93*, 1702−1708.
(41) Wu, C.; Huang, S.; Wang, Y.; Chai, Y.; Yuan, R.; Yang, X. *Anal. Chem.* **2021**, *93*, 11019−11024.
(42) Yang, X.; Wang, S.; Wang, Y.; He, Y.; Chai, Y.; Yuan, R. *ACS Appl. Mater. Interfaces* **2018**, *10*, 12491−12496.
(43) Zhu, L.; Miao, M.; Shao, X.; Du, Z.; Huang, K.; Luo, Y.; Xu, W. *Anal. Chem.* **2019**, *91*, 14992−14999.
(44) Broman, A.; Lenshof, A.; Evander, M.; Happonen, L.; Ku, A.; Malmström, J.; Laurell, T. *Anal. Chem.* **2021**, *93*, 3929−3937.
(45) Fu, P.; Xing, S.; Xu, M.; Zhao, Y.; Zhao, C. *Sens. Actuators, B* **2020**, *305*, No. 127545.

NOTE ADDED AFTER ASAP PUBLICATION

This paper was published ASAP on March 15, 2022, with errors in Figures 2, 3, 4, and 5 and Figure S7 in the Supporting Information. The corrected version was reposted on March 28, 2022.

https://doi.org/10.1021/acs.analchem.1c05200
Anal. Chem. 2022, 94, 6967−6975